Molecular Simulations Reveal the Free Energy Landscape and Transition State of Membrane Electroporation

Gari Kasparyan and Jochen S. Hub*
Theoretical Physics and Center for Biophysics, Saarland University, 66123 Saarbrücken, Germany

(Received 5 February 2023; accepted 29 February 2024; published 4 April 2024)

The formation of pores over lipid membranes by the application of electric fields, termed membrane electroporation, is widely used in biotechnology and medicine to deliver drugs, vaccines, or genes into living cells. Continuum models for describing the free energy landscape of membrane electroporation were proposed decades ago, but they have never been tested against spatially detailed atomistic models. Using molecular dynamics (MD) simulations with a recently proposed reaction coordinate, we computed potentials of mean force of pore nucleation and pore expansion in lipid membranes at various transmembrane potentials. Whereas the free energies of pore expansion are compatible with previous continuum models, the experimentally important free energy barrier of pore nucleation is at variance with established models. The discrepancy originates from different geometries of the transition state; previous continuum models assumed the presence of a membrane-spanning defect throughout the process, whereas, according to the MD simulations, the transition state of pore nucleation is typically passed before a transmembrane defect has formed. A modified continuum model is presented that qualitatively agrees with the MD simulations. Using kinetics of pore opening together with transition state theory, our free energies of pore nucleation are in excellent agreement with previous experimental data.

DOI: 10.1103/PhysRevLett.132.148401

Membrane electroporation is routinely used to form pores in the lipid membrane of biological cells [1–3]. The technique enables the delivery of cargos such as vaccines, drug, genes, or dyes into cells for a wide range of applications in biology, biotechnology, medicine, and food technology [4–6]. The exposure of cells to short electric pulses typically leads to reversible electroporation as the pore may reseal spontaneously [7,8]. Longer or stronger pulses lead to irreversible electroporation and cell death as used for ablating malignant tumors that are not accessible for surgery [9,10].

Electroporation has frequently been modeled assuming two distinct lipid arrangements [1,11,12]. Accordingly, during pore nucleation, a hydrophobic pore is formed that is characterized by the protrusion of a thin water needle into the membrane core. As the pore radius expands, the lipid headgroups reorient to shield the aqueous defect from the hydrophobic membrane core, thereby forming a hydrophilic pore. Continuum theories for modeling the free energy landscape of this process have been considered mature since the late 1980s [7]. The established theory describes the hydrophobic pore as a membrane-spanning cylinder with an unfavorable free energy due to the surface tension at the cylindrical water-membrane interface. The free energy of the hydrophilic pore involves a radius-dependent line tension along the pore rim accounting for the cost for reorienting the lipid headgroups and for the unfavorable lipid packing at the rim [6]. The free energy landscape predicted by this continuum theory has, to the best of our knowledge, never been compared with predictions from spatially more detailed atomistic models.

Molecular dynamics (MD) simulations have been crucial for obtaining atomic insight into membrane electroporation [13–18]. MD simulations confirmed the occurrence of hydrophobic and hydrophilic pores during pore formation, while the radii of stable open pores were in good agreement with experimental estimates [18]. The effect of lipid composition on pore formation has been investigated in detail by simulations [19–23]. To induce pores within accessible simulation times, pores have been formed under excessive nonequilibrium conditions by applying large transmembrane potentials of several volts, which would lead to membrane rupture after a pore has nucleated. However, because good reaction coordinates (RCs) for driving pore formation were not available until recently, MD simulation did not lead to understanding of the free energy landscape of pore formation. Such understanding would be highly valuable to design electric pulses with the desired effects on membranes [24], to rationalize the kinetics of pore opening and closing under conditions of different potentials or different lipid compositions [8,25], or to translate results found for model membranes into complex biological membranes [23]. Here, we closed this gap and computed the free energy landscape of electroporation covering pore nucleation and expansion at experimentally relevant potentials.

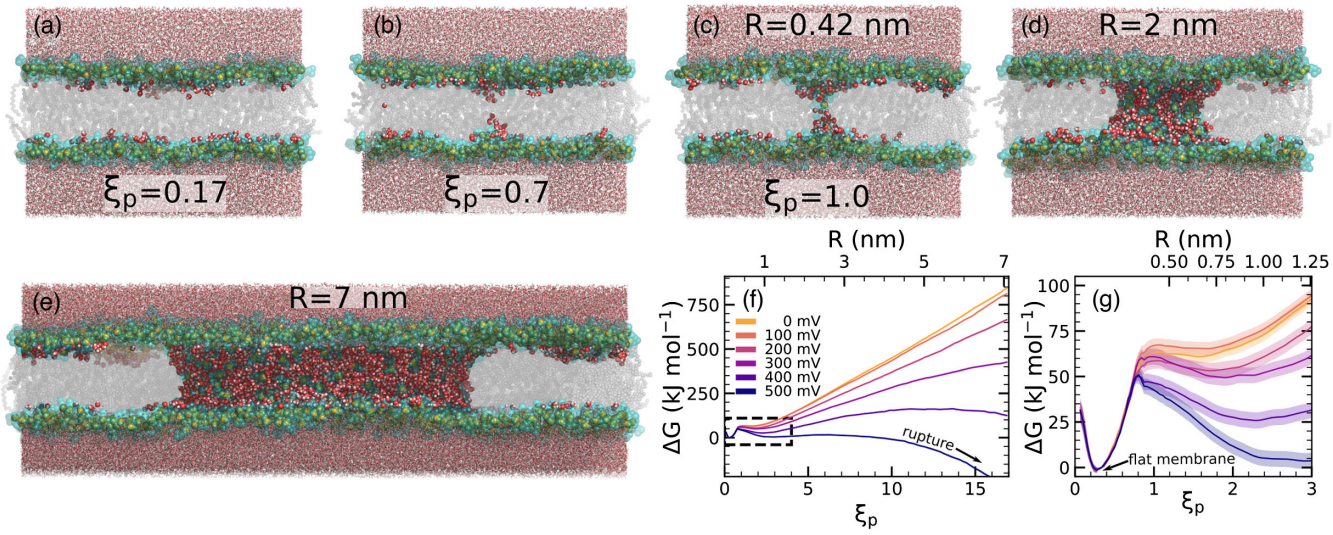

FIG. 1. (a)–(c) Simulation snapshots of pore nucleation and (c)–(e) pore expansion. Lipid headgroups are shown as green spheres, tails in gray, water within the membrane as red and white spheres, and other water as red and white sticks. The respective positions along the reaction coordinate ξ_p and pore radius R are shown in the panels. (f),(g) Potentials of mean force (PMFs) for pore nucleation and pore expansion across a DPPC membrane at transmembrane voltages between 0 and 500 mV [for color code see panel (f)]. Lower and upper abscissas show the reaction coordinate and the pore radius, respectively. The dashed box in panel (f) indicates the region highlighted in panel (g).

Potentials of mean force (PMFs) were computed along a recently proposed RC ξ_p for pore nucleation and expansion [26]. For $\xi_p \lessapprox 1$, the RC quantifies the degree of connectivity of a polar transmembrane defect [Figs. 1(a)–1(c)] [27]; for $\xi_p \gtrapprox 1$, the RC quantifies the pore radius R in units of the radius $R_0 \approx 0.4\,\mathrm{nm}$ of a fully nucleated pore, i.e., $\xi_\mathrm{p} = R/R_0$ [Figs. 1(c)–1(e)]. The transition between nucleation and expansion is implemented with a differentiable switch function (see Supplemental Material [SM] Methods [28]). We showed previously that PMF calculations with this RC converge rapidly and are not compromised by hysteresis problems [26,27,53].

Figures 1(f) and 1(g) present PMFs for electroporation across a membrane of dipalmitoylphosphatidylcholine (DPPC) at transmembrane potentials U between 0 and 500 mV, modeled with the force field by Berger *et al.* [54]. The PMFs reveal a free energy cost of 50 to 65 kJ/mol for the formation of a thin water needle as required for pore nucleation. The presence of free energy minima around $R \sim 0.8\,\mathrm{nm}$ demonstrates the presence of metastable, long-living pores for voltages $U \leq 500\,\mathrm{mV}$, while this free energy minimum is very shallow at zero voltage [Fig. 1(f), yellow]. With increasing voltage, the minimum becomes more pronounced and is shifted to larger R, indicating that the metastable pores exhibit increasing lifetime and conductivity. At $U \geq 500\,\mathrm{mV}$, the PMFs exhibit no significant barrier against further expansion [Figs. 1(f) and 1(g), dark blue], suggesting that the pores spontaneously further expand leading to membrane rupture. Free simulations confirmed that pores are metastable at intermediate voltages, whereas pores spontaneously close or expand at small or large voltages, respectively, in agreement with the PMFs (Supplemental Material, Figs. S8 and S9).

Continuum theories of pore expansion suggest that the transmembrane potential modifies the pore free energy by the electrostatic energy $E_\mathrm{c} = -\Delta C U^2/2$, where the change of the capacitance of the membrane is $\Delta C = (\varepsilon_w - \varepsilon_m)\pi R^2/d$. Here, ε_w and ε_m denote the dielectric permittivity of water and of the membrane core, and d is the thickness of the membrane. For the regime of pore expansion ($\xi_p > 1$), the PMFs are in agreement with the continuum model of pore expansion as the free energies for fixed pore radii decrease with U^2 (Fig. S1B), while the PMFs at various voltages are decreased relative to the PMF at zero voltage following mainly a quadratic R^2 dependence (Fig. S1C). Hence, for fully established nanometer-sized pores, the continuum model captures the trends obtained from the MD simulations.

During pore nucleation, however, polar defects with diameters of only few angstroms protrude the membrane, suggesting that the finite size of water molecules becomes relevant. To reveal how the free energy barrier and the transition state (TS) for pore nucleation depend on the voltage, we computed PMFs of pore nucleation across a DPPC membrane using voltages between 0 mV and 1900 mV [Fig. 2(a)]. The PMFs were computed along the chain reaction coordinate ξ_ch, which is a measure for the degree of connectivity of the defect and which is equivalent to ξ_p for $\xi_p < 0.9$ (SM Methods). Here, $\xi_\mathrm{ch} \approx 0.3$ corresponds to the flat unperturbed membrane [Fig. 1(a)],

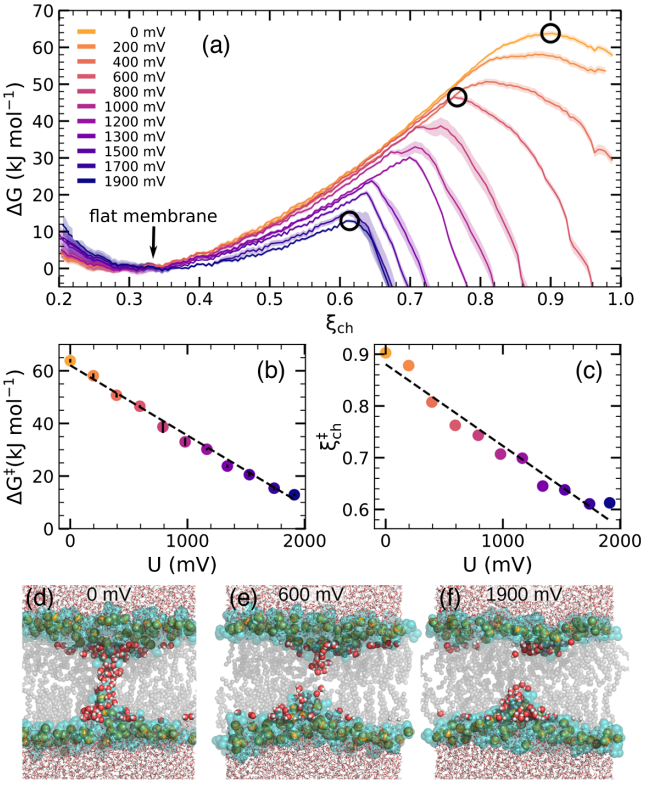

FIG. 2. (a) PMFs of pore nucleation at transmembrane voltages U between 0 and 1900 mV (see legend) as a function of the chain coordinate ξ_{ch}, which quantifies the connectivity of the transmembrane defect. (b) Free energy barrier for pore nucleation as taken from the maxima of the PMFs in panel (a). (c) Position of ξ_{ch} at the transition state. Dashed lines in panels (b) and (c) are linear fits to guide the eye. (d)–(f) MD snapshots of the transition state for voltages of 0 mV, 600 mV, or 1900 mV [panel (a), black circles], characterized by discontinuous partial defects for $U \geq 600$ mV.

whereas $\xi_{ch} \approx 0.9$ indicates a membrane-spanning polar defect [Fig. 2(d)]; pore expansion is not resolved by ξ_{ch} since larger pores are projected onto $\xi_{ch} = 1$.

The PMFs in Fig. 2(a) demonstrate that the free energy landscape of pore nucleation is greatly modulated by transmembrane voltages. With increasing U, the barrier of the PMFs, corresponding to the TS of pore nucleation, is shifted to smaller free energies and to smaller values of ξ_{ch}. Specifically, the barrier height $\Delta G^{\ddagger}$ of the TS decreases approximately linearly with U [Fig. 2(b)]. Hence, not only the open pore is stabilized by the potential, but the kinetics of pore formation are greatly accelerated. Assuming transition state theory (TST), the rate of pore nucleation follows $\exp(-\beta \Delta G^{\ddagger})$, where β is the inverse temperature; according to TST, the decrease of the barrier from 64 kJ/mol to 13 kJ/mol upon the application of 1900 mV implies that the rate of pore formation is accelerated by approximately 8 orders of magnitude. The linear decay of $\Delta G^{\ddagger}$ with U is at variance with widely accepted continuum models discussed below [6,11,12,25,55,56]; however, the linear decay agrees with recent experiments [57] and has been proposed by Böckmann *et al.* by extrapolating kinetics of pore formation observed in MD simulation at large potentials towards experimental kinetics at small potentials [18].

The position of the TS along the reaction coordinate, $\xi^{\ddagger}_{ch}$, is shifted to smaller values with increasing voltage [Fig. 2(c)]. Since ξ_{ch} quantified the degree of connectivity of the defect, these findings imply that, with increasing potential, the TS is characterized by a decreasingly connected polar defect. Whereas the TS for 0 mV represents a continuous transmembrane defect [Fig. 2(d)], the TSs for higher potentials exhibit only partial water protrusions that span the membrane incompletely [Figs. 2(e) and 2(f), S2, S3]. Hence, during pore nucleation at higher potentials, the TS is passed *before* a continuous transmembrane needle has formed. This finding suggests that previous continuum models, which modeled the entire pore formation process using transmembrane cylinders with increasing radii, were not capable of modeling the TS at higher potentials.

The discrepancy between MD simulation and previous continuum models is explained by different geometries of the TS. Whereas previous continuum models assumed membrane-spanning water cylinders throughout the pore formation process, MD simulations suggest that, at higher potentials, the TS is passed before a continuous defect has formed. Hence, we devised a modified continuum model involving a gradual formation of a transmembrane defect and, thereby, capable of capturing the TS of pore nucleation. We model the growing defect as three capacitors in series, where the upper and lower cylinder-shaped capacitors of height $h/2$ are filled by water, whereas the central capacitor is filled by lipid tails [Figs. 3(a) and S5]. As detailed in Supplemental Material Sec. II, the free energy change upon protrusion of the two water cylinders is

$$\Delta G(\xi, U) = 2\pi r_w d \Gamma_{\mathrm{eff}} \xi - \frac{1}{2} C_0 U^2 \frac{\xi}{\tilde{\epsilon} - \xi}, \tag{1}$$

where r_w is the constant radius of the cylinder, Γ_{eff} the surface tension between water and lipid tails, C_0 the capacitance of a purely hydrophobic cylinder, $\tilde{\epsilon} = \epsilon_w/(\epsilon_w - \epsilon_m)$, and $\xi = h/d \in [0, 1]$ the degree of connectivity of the defect, similar to the chain coordinate ξ_{ch} used in the PMF calculations of pore nucleation. Figure 3(b) presents $\Delta G(\xi, U)$ curves for potentials between 0 and 4500 mV, revealing a decreasing TS free energy $\Delta G^{\ddagger}$ and a decreasing position $\xi^{\ddagger}$ with increasing potential, in qualita tive agreement with the PMFs from MD simulations [Figs. 2(a)–2(c)]. The transition state, given by the maxima of the $\Delta G(\xi, U)$ curves, is at

$$\xi^{\ddagger} = \tilde{\epsilon}\left[1 - \sqrt{C_0/2\tilde{\epsilon}G_s}U\right] \tag{2}$$

$$\Delta G^{\ddagger} \approx \tilde{\epsilon} G_s \left[1 - \sqrt{C_0/2\tilde{\epsilon}G_s}U\right], \tag{3}$$

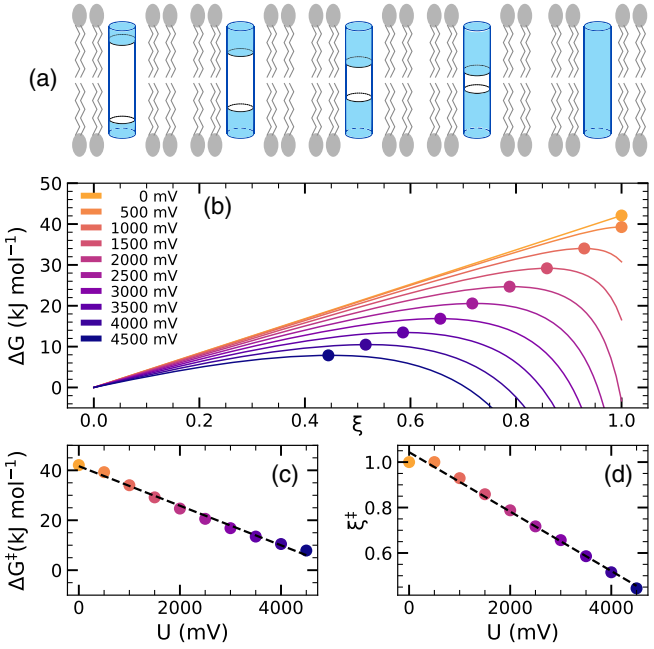

FIG. 3. Energetics of pore nucleation by the three-cylinder continuum model. (a) Gradual formation of a transmembrane defect modeled by three cylindrical capacitors in series. (b) Free energy profiles of pore nucleation for transmembrane voltages between 0 and 4500 mV (for color code, see legend); (c) free energy barrier and (d) position of the transition state [colored dots in panel (b)].

where $G_s = 2\pi r_w d\Gamma_{\mathrm{eff}}$ denotes the surface tension free energy of a membrane-spanning water-filled cylinder. Hence, $\xi^{\ddagger}$ and $\Delta G^{\ddagger}$ decrease linearly with the potential [Figs. 3(b) and 3(c)], in agreement with the findings from the PMFs [Figs. 2(b) and 2(c)], suggesting that the model accounts for the correct geometry of pore nucleation and for the dominating energetic contributions.

Nevertheless, the thee-cylinder model is simplified as it neglects several contributions to the free energies. First, local elastic thinning of the membrane may stabilize the early water protrusions, which may explain the quadratic free energy increase in the PMFs [Fig. 2(a), $\xi_{\mathrm{ch}} \approx 0.3$] in contrast to the linear increase proposed by the three-cylinder model [Fig. 3(b), $\xi \approx 0$]. Second, during the MD simulations, individual lipid headgroups frequently followed the water protrusions far into the membrane core, even before continuous transmembrane defect has formed; owing to the large permittivity of the headgroup region [58], such headgroups may increase the overall permittivity of the defect, thereby increasing the electrostatic stabilization E_c of the pore at the cost of some lipid deformation energy. Such effects may rationalize why $\Delta G^{\ddagger}$ decays more rapidly with U in the simulations as compared to the three cylinder model [Figs. 2(b) and 3(c)]. Early occasional protrusions of individual headgroups further explain why the MD simulations do not reveal an instantaneous transition from a hydrophobic to a hydrophilic pore, as anticipated by the previous continuum model (Fig. S4B), but instead a gradual transition from a water needle stabilized by local membrane thinning towards a fully established toroidal pore, as illustrated in Supplemental Movies S1–S6.

Since the PMFs of pore nucleation exhibit a single barrier [Figs. 1(f) and 2(a)], we used TST to describe the rate of pore opening by $k_{\mathrm{o}} = \kappa \exp(-\beta \Delta G^{\ddagger})$, where κ is the attempt frequency. We estimated the attempt frequency κ from a series of free MD simulations starting with a planar membrane. Within 20 1-μs simulations each at potentials of 1500 mV, 1700 mV, or 1900 mV, we observed 1, 9, or 19 opening events within simulation time, respectively. Using a maximum-likelihood estimate, we obtained the rates k_{o} of pore opening for these voltages (SM Methods, Table SII) and, together with the respective free energy barriers [Fig. 2(a)], the attempt frequency via $\kappa = k_{\mathrm{o}} \exp(+\beta \Delta G^{\ddagger})$. The attempt frequencies estimated from simulations at different voltages were in reasonable agreement (Table SII) suggesting that TST is applicable and yielding an attempt frequency of $\kappa \approx 0.25\,\mathrm{ns}^{-1}$, corresponding to roughly one attempt per 4 ns.

Notably, the attempt frequency of $0.25\,\mathrm{ns}^{-1}$ is approximately 3 orders of magnitude smaller as compared to a previous estimate based on the number of lipid collisions [59]. Instead, the time of ∼4 ns per attempt corresponds approximately to the time required for lipids to diffuse a typical lipid-lipid distance and, therefore, may be taken as a timescale of lipid-lipid rearrangements. A similar attempt frequency of $\sim 0.3\,\mathrm{ns}^{-1}$ was previously derived for describing the kinetics of stalk formation with TST [60]. This suggests that lipid-lipid rearrangements, rather than lipid collisions, may be interpreted as attempts of large-scale topological transitions of membranes such as pore formation or stalk formation in the context of TST.

Having established the attempt frequency of pore formation, TST enables estimates of pore opening rates for voltages that do not trigger spontaneous pore opening in free simulations within acceptable simulations times. Following such strategy, we validated the MD simulations of pore formation against experimental data by Melikov *et al.* [8], who reported mean times of pore opening across black lipid membranes of diphytanoyl phosphatidylcholine (DPhPC) at voltages between 250 mV and 550 mV. To this end, we computed PMFs of pore nucleation across a membrane of DPhPC at voltages between 0 mV and 1200 mV using the Charmm36 force field [Fig. 4(a), SM Methods [28]] [61]. From the free energy of the pore ($\xi_{\mathrm{ch}} \approx 0.9$) or from the free energy barrier (if present) together with TST, we computed the mean time of pore opening τ_{o} for a circular black lipid membrane with radius of 150 μm [8]. The mean pore opening times τ_{o} from the MD simulations are in good agreement with experimental data both in terms of the magnitude and in terms of the

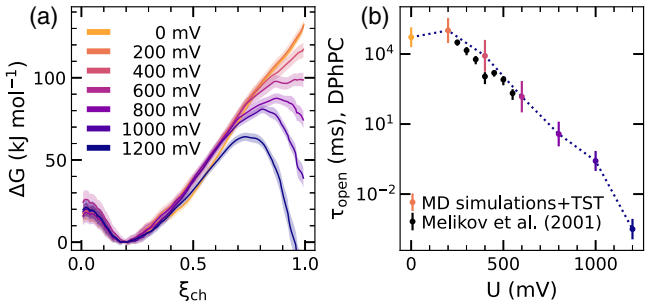

FIG. 4. (a) PMFs of pore nucleation in a DPhPC membrane at voltages between 0 mV and 1200 mV (see legend). (b) Mean time of pore opening derived from MD simulations based on transition state theory and using the pore free energies (or free energy barriers, if present) in panel (a) (colored dots). Black dots: Experimental data by Melikov *et al.* [8].

voltage dependence of τ_o [Fig. 4(b)]. The agreement is remarkable considering that neither the applied Charmm36 force field has been refined against free energies of pore opening nor any other fitting has been applied for this comparison between simulation and experiment.

To conclude, we derived the free energy landscape of membrane electroporation from all-atom MD simulations, involving both pore nucleation and pore expansion. We showed that previous continuum theories, which modeled pore formation purely based on a continuous transmembrane water cylinder, are in good agreement with the MD-based PMFs only in the pore expansion regime, that is, after a continuous transmembrane defect has formed. However, previous models failed to explain the free energy and structure of the TS of pore nucleation because, according to the MD simulations at higher potentials, the TS is passed before a membrane-spanning defect has formed. We presented a continuum model of pore nucleation that agrees qualitatively with the MD-based PMFs of pore nucleation. Finally, using TST together with (i) an attempt frequency corresponding to the timescale of lipid-lipid rearrangements and (ii) free energies from the PMFs, we derived pore opening times in quantitative agreement with previous experimental data. The comparison of pore formation kinetics between simulation and experiments validates not only the PMF calculation protocol, but furthermore provides a new means for testing the accuracy of lipid force fields under large-scale membrane conformational transitions. Together, this study provided energetic and structural insight into membrane electroporation and paves the way for interpreting and designing electroporation applications in biotechnology and medicine.

This study was supported by Deutsche Forschungsgemeinschaft (DFG, German Research Foundation; Grants No. SFB 803/A12, No. SFB 1027/B7, and No. INST 256/539-1).

*jochen.hub@uni-saarland.de

[1] I. G. Abidor, V. B. Arakelyan, L. V. Chernomordik, Y. A. Chizmadzhev, V. F. Pastushenko, and M. R. Tarasevich, J. Electroanal. Chem. **104**, 37 (1979).
[2] R. Benz, F. Beckers, and U. Zimmermann, J. Membr. Biol. **48**, 181 (1979).
[3] L. V. Chernomordik, M. M. Kozlov, G. B. Melikyan, I. G. Abidor, V. S. Markin, and Y. A. Chizmadzhev, Biochim. Biophys. Acta **812**, 643 (1985).
[4] M. Golzio, J. Teissie, and M.-P. Rols, Proc. Natl. Acad. Sci. U.S.A. **99**, 1292 (2002).
[5] L. Lambricht, A. Lopes, S. Kos, G. Sersa, V. Préat, and G. Vandermeulen, Expert Opin. Drug Delivery **13**, 295 (2016).
[6] T. Kotnik, L. Rems, M. Tarek, and D. Miklavčič, Annu. Rev. Biophys. **48**, 63 (2019).
[7] R. W. Glaser, S. L. Leikin, L. V. Chernomordik, V. F. Pastushenko, and A. I. Sokirko, Biochim. Biophys. Acta **940**, 275 (1988).
[8] K. C. Melikov, V. A. Frolov, A. Shcherbakov, A. V. Samsonov, Y. A. Chizmadzhev, and L. V. Chernomordik, Biophys. J. **80**, 1829 (2001).
[9] K. N. Aycock and R. V. Davalos, Bioelectricity **1**, 214 (2019).
[10] B. Geboers, H. J. Scheffer, P. M. Graybill, A. H. Ruarus, S. Nieuwenhuizen, R. S. Puijk, P. M. van den Tol, R. V. Davalos, B. Rubinsky, T. D. de Gruijl *et al.*, Radiology **295**, 254 (2020).
[11] J. C. Weaver and Y. A. Chizmadzhev, Bioelectrochem. Bioenerg. **41**, 135 (1996).
[12] J. C. Neu and W. Krassowska, Phys. Rev. E **59**, 3471 (1999).
[13] D. P. Tieleman, BMC Biochem **5**, 10 (2004).
[14] M. Tarek, Biophys. J. **88**, 4045 (2005).
[15] A. A. Gurtovenko and I. Vattulainen, J. Am. Chem. Soc. **127**, 17570 (2005).
[16] Q. Hu, S. Viswanadham, R. P. Joshi, K. H. Schoenbach, S. J. Beebe, and P. F. Blackmore, Phys. Rev. E **71**, 031914 (2005).
[17] P. T. Vernier, M. J. Ziegler, Y. Sun, W. V. Chang, M. A. Gundersen, and D. P. Tieleman, J. Am. Chem. Soc. **128**, 6288 (2006).
[18] R. A. Böckmann, B. L. De Groot, S. Kakorin, E. Neumann, and H. Grubmüller, Biophys. J. **95**, 1837 (2008).
[19] M. J. Ziegler and P. T. Vernier, J. Phys. Chem. B **112**, 13588 (2008).
[20] A. A. Gurtovenko, J. Anwar, and I. Vattulainen, Chem. Rev. **110**, 6077 (2010).
[21] T. J. Piggot, D. A. Holdbrook, and S. Khalid, J. Phys. Chem. B **115**, 13381 (2011).
[22] L. Delemotte and M. Tarek, J. Membr. Biol. **245**, 531 (2012).
[23] L. Rems, X. Tang, F. Zhao, S. Pérez-Conesa, I. Testa, and L. Delemotte, eLife **11**, e74773 (2022).
[24] P. Mukherjee, C. A. Patino, N. Pathak, V. Lemaitre, and H. D. Espinosa, Small **18**, 2107795 (2022).
[25] J. T. Sengel and M. I. Wallace, Proc. Natl. Acad. Sci. U.S.A. **113**, 5281 (2016).
[26] J. S. Hub, J. Chem. Theory Comput. **17**, 1229 (2021).
[27] J. S. Hub and N. Awasthi, J. Chem. Theory Comput. **13**, 2352 (2017).

[28] See Supplemental Material at http://link.aps.org/supplemental/10.1103/PhysRevLett.132.148401 for reviews of the established continuum model of electroporation, the derivation of the new three-cylinder model, computational details, Figs. S1–S9, and Tables SI–SII. It contains Refs. [29–52].
[29] K. A. DeBruin and W. Krassowska, Biophys. J. **77**, 1213 (1999).
[30] C. J. Knight and J. S. Hub, Bioinformatics **31**, 2897 (2015).
[31] H. J. C. Berendsen, J. P. M. Postma, W. F. van Gunsteren, and J. Hermans, in *Intermolecular Forces*, edited by B. Pullman (D. Reidel Publishing Company, Dordrecht, 1981), pp. 331–342.
[32] M. J. Abraham, T. Murtola, R. Schulz, S. Páll, J. C. Smith, B. Hess, and E. Lindahl, SoftwareX **1**, 19 (2015).
[33] G. Bussi, D. Donadio, and M. Parrinello, J. Chem. Phys. **126**, 014101 (2007).
[34] M. Bernetti and G. Bussi, J. Chem. Phys. **153**, 114107 (2020).
[35] T. Darden, D. York, and L. Pedersen, J. Chem. Phys. **98**, 10089 (1993).
[36] U. Essmann, L. Perera, M. L. Berkowitz, T. Darden, H. Lee, and L. G. Pedersen, J. Chem. Phys. **103**, 8577 (1995).
[37] S. Miyamoto and P. A. Kollman, J. Comput. Chem. **13**, 952 (1992).
[38] B. Hess, J. Chem. Theory Comput. **4**, 116 (2008).
[39] B. Roux, Biophys. J. **95**, 4205 (2008).
[40] J. Melcr, D. Bonhenry, Š. Timr, and P. Jungwirth, J. Chem. Theory Comput. **12**, 2418 (2016).
[41] G. Kasparyan and J. S. Hub, J. Chem. Theory Comput. **19**, 2676 (2023).
[42] J. B. Klauda, R. M. Venable, J. A. Freites, J. W. O'Connor, D. J. Tobias, C. Mondragon-Ramirez, I. Vorobyov, A. D. MacKerell, Jr, and R. W. Pastor, J. Phys. Chem. B **114**, 7830 (2010).
[43] C. W. Hopkins, S. Le Grand, R. C. Walker, and A. E. Roitberg, J. Chem. Theory Comput. **11**, 1864 (2015).
[44] W. L. Jorgensen, J. Chandrasekhar, J. D. Madura, R. W. Impey, and M. L. Klein, J. Chem. Phys. **79**, 926 (1983).
[45] G. M. Torrie and J. P. Valleau, Chem. Phys. Lett. **28**, 578 (1974).
[46] N. Awasthi and J. S. Hub, in *Biomembrane Simulations. Computational Studies of Biological Membranes* (CRC Press, Taylor & Francis Group, Boca Raton, 2019).
[47] N. Awasthi, W. Kopec, N. Wilkosz, D. Jamróz, J. S. Hub, M. Zatorska, R. Petka, M. Nowakowska, and M. Kepczynski, ACS Biomater. Sci. Eng. **5**, 780 (2019).
[48] G. Kasparyan, C. Poojari, T. Róg, and J. S. Hub, J. Phys. Chem. B **124**, 8811 (2020).
[49] S. F. Verbeek, N. Awasthi, N. K. Teiwes, I. Mey, J. S. Hub, and A. Janshoff, Eur. Biophys. J. **50**, 127 (2021).
[50] S. Kumar, D. Bouzida, R. H. Swendsen, P. A. Kollman, and J. M. Rosenberg, J. Comput. Chem. **13**, 1011 (1992).
[51] J. S. Hub, B. L. de Groot, and D. van der Spoel, J. Chem. Theory Comput. **6**, 3713 (2010).
[52] M. L. Fernández, M. Risk, R. Reigada, and P. T. Vernier, Biochem. Biophys. Res. Commun. **423**, 325 (2012).
[53] N. Awasthi and J. S. Hub, J. Chem. Theory Comput. **12**, 3261 (2016).
[54] O. Berger, O. Edholm, and F. Jähnig, Biophys. J. **72**, 2002 (1997).
[55] C. Chen, S. Smye, M. Robinson, and J. Evans, Med. Biol. Eng. Comput. **44**, 5 (2006).
[56] D. L. Perrier, L. Rems, and P. E. Boukany, Adv. Colloid Interface Sci. **249**, 248 (2017).
[57] E. J. Lafarge, P. Muller, A. P. Schroder, E. Zaitseva, J. C. Behrends, and C. M. Marques, Proc. Natl. Acad. Sci. U.S.A. **120**, e2213112120 (2023).
[58] H. A. Stern and S. E. Feller, J. Chem. Phys. **118**, 3401 (2003).
[59] Z. Vasilkoski, A. T. Esser, T. R. Gowrishankar, and J. C. Weaver, Phys. Rev. E **74**, 021904 (2006).
[60] C. S. Poojari, K. C. Scherer, and J. S. Hub, Nat. Commun. **12**, 6594 (2021).
[61] R. Pastor and A. MacKerell Jr., J. Phys. Chem. Lett. **2**, 1526 (2011).